Titan's topography and shape at the end of the Cassini mission

P. Corlies[1], A.G. Hayes[1], S.P.D. Birch[1], R. Lorenz[2]. B.W. Stiles[3], R. Kirk[4].

V. Poggiali[1], H. Zebker[5], L. Iess[6]

Paul Corlies, pcorlies@astro.cornell.edu

[1]Department of Astronomy, Cornell University, Ithaca, New York, USA.

[2]Applied Physics Lab, Johns Hopkins University, Laurel, Maryland, USA.

[3]Jet Propulsion Laboratory, California Institute of Technology, Pasadena, California, USA.

[4]United States Geological Survey Astrogeology Division, Flagstaff, Arizona, USA.

This article has been accepted for publication and undergone full peer review but has not been through the copyediting, typesetting, pagination and proofreading process, which may lead to differences between this version and the Version of Record. Please cite this article as doi: 10.1002/2017GL075518

With the conclusion of the Cassini mission, we present an updated topographic map of Titan, including all the available altimetry, SARtopo, and stereo-photogrammetry topographic datasets available from the mission. We use radial basis functions to interpolate the sparse dataset, which covers only ∼9% of Titan's global area. The most notable updates to the topography include higher coverage of the poles of Titan, improved fits to the global shape, and a finer resolution of the global interpolation. We also present a statistical analysis of the error in the derived products and perform a global minimization on a profile-by-profile basis to account for observed biases in the input dataset. We find a greater flattening of Titan than measured, additional topographic rises in Titan's southern hemisphere, and better constrain the possible locations of past and present liquids on Titan's surface.

Keypoints:

• Updated topographic and spherical harmonic maps of Titan using three times more interpolation points

[5]Departments of Geophysics and
Electrical Engineering, Stanford University,
Stanford, California, USA.

[6]Dipartimento di Ingegneria Meccanica e
Aerospaziale, Sapienza Universita di Roma,
Rome, Italy.

- All maps are electronically available for use by the community
- An additional mountain and topographic influences on liquid distributions are observed

1. Introduction

Topographic data are essential to understanding and deciphering the stratigraphic relationships and process-interactions that lead to the development of landscapes on Earth and other worlds. Titan is no exception and plays hosts to a variety of geophysical and meteorological processes including aeolian dunes [*Radebaugh et al.*, 2008; *Lorenz and Radebaugh*, 2009], fluvial networks [*Lorenz et al.*, 2008; *Burr et al.*, 2013], lacustrine processes [*Stofan et al.*, 2007; *Hayes et al.*, 2008], tectonic activity [*Radebaugh et al.*, 2007; *Cartwright et al.*, 2011], and convective clouds [*Griffith et al.*, 2009; *Rafkin and Barth*, 2015], all of which can be influenced by the local and/or global topography. Further, comparisons between gravity and shape measurements can better constrain Titan's interior structure [*Nimmo and Bills*, 2010]. Thus, obtaining the most accurate map of Titan's topography and shape is important for understanding the mechanisms that drive these processes.

The first spherical harmonic analysis of Titan's shape came from *Zebker et al.* [2009a] but suffered from a lack of coverage over Titan's South Pole. To correct for this deficit, a nuisance parameter was included to not allow estimates to deviate significantly from a sphere. *Mitri et al.* [2014] improved upon the estimate of Titan's shape, using similar techniques as *Zebker et al.* [2009a], but with greater global coverage, finding an overall flatter estimate of Titan's shape. Complementing these efforts, *Lorenz et al.* [2013] made the first fit of Titan's topography using bicubic splines of SARtopo/altimetry data from TA-T77. Building on these previous efforts, we present here an updated topographic map of Titan, now making use of all available data from the now-completed Cassini mission.

While we provide initial context for some of the most interesting features observed, we leave detailed studies of geological, hydrological, and meteorologic implications of the new topography to future work. Our topographic products are available in the Supplementary Online Material (SOM) of this manuscript.

2. Methods

There are a variety of well established interpolation schemes for handling sparsely and non-uniformly sampled data, such as Titan's topography. In this section, we present the data and interpolation methods used as well as a description of the error analysis of our final product.

2.1. Topographic Data

Topographic data of Titan are derived from the Cassini RADAR [*Elachi et al.*, 2004] using three methods: SARtopo, altimetry, and stereo-photogrammetry. SARtopo makes use of the relative return between overlapping regions of the Cassini RADAR beams to make an estimate of the local topography [*Stiles et al.*, 2009]. Altimetry employs a time-of-flight measurement through a nadir viewing geometry to accurately measure the distance to the surface [*Zebker et al.*, 2009b]. Finally, stereo-photogrammetry uses the spacecraft position and viewing geometry to triangulate features observed in multiple SAR images to determine their location on Titan's surface [*Kirk et al.*, 2012].

The SARtopo data consists of 122 profiles covering ∼5.2% of Titan's surface with an average error in elevation of ∼160m over all 122 profiles. The altimetry data are comprised of 69 profiles covering an additional ∼1.6% of Titan's surface. Although altimetry provides a much smaller coverage compared to SARtopo, the vertical error is only ∼35m

[*Zebker et al.*, 2009b]. Finally, 19 digital terrain models (DTMs) made through stereo photogrammetry cover an additional ∼2.1%, with a typical error of ∼100m [*Kirk et al.*, 2012].

Before the creation of the final topographic interpolation, each dataset was cleaned to remove outliers and erroneous data. For both datasets, data acquired outside a 4km elevation range of [-2000m to 2000m] were removed, as this is the range of elevations considered when deriving SARtopo data products [*Stiles et al.*, 2009] and encompasses the majority of elevations from radarclinometry used to derive mountain heights [*Radebaugh et al.*, 2007]. SARtopo data were further cleaned by removing: any footprint with an incident angle less than 10° [*Stiles et al.*, 2009], any footprint whose error was 2σ greater than the average systematic error, as well as any footprint that overlapped with one of Titan's seas (and including Ontario Lacus) by more than 30%. Altimetry data were further cleaned by excluding any footprints with off-nadir angles greater than .2° degrees, the size of the RADAR's 3dB gain pattern, as well as any footprint whose measured SNR was 20dB less than the average (i.e. a 1% threshold). No bias corrections were applied to correct for the small mispointings in the altimeter, as these are small compared to the assumed error of 35m for the altimeter. Finally, the DTMs, provided by the USGS, were cleaned using the co-registration-figure-of-merit and and through a by-eye correlation of the DTMs to the associated SAR imaging to remove any DTMs that gave non-physical results. A final by-hand cleaning was then done to remove isolated points or erroneous values at the beginning or ends of swaths, where the measured topography is more uncertain.

2.2. Interpolation Scheme

Because of the limited coverage of the data, an interpolation must be used to generate a complete global map of Titan's topography. There are many interpolation techniques available: spline with tension (as used in [*Lorenz et al.*, 2013]), inverse distance weighting, nearest neighbors, kriging interpolation [*Krige*, 1951; *Matheron*, 1963], or radial basis functions (RBFs) [*Powell*, 1977; *Broomhead and Lowe*, 1988]. We have chosen here to use RBFs for interpolating the global topography because of their flexibility and ease of computation.

RBFs use a network of radially symmetric functions centered at nodes, whose locations are defined by the observed data, which are then summed to generate a global approximation of the topography. The distance from the node is defined as the Euclidean norm between observations in the projection space. We have chosen to use linear basis functions for the global interpolation. Their smooth dependence with distance minimizes the influence of any localized variations on global scales. Finally, to correct for projection effects in the polar regions we interpolate the poles in a stereographic projection and then combine them with the global projection to allow for consistent and well behaved data across the poles. There is no additional smoothing in the data, in order to remain as true to the data as possible. Interpolation on coarser scales or with high-frequency filtered data would further remove fine scale variations. More details on the interpolation scheme can be found in the SOM [*Rippa*, 1999].

2.3. Minimization

SARtopo data are initially globally adjusted with respect to the viewing geometries of each Titan flyby from Ta-T121 [*Stiles et al.*, 2009] in order to minimize relative off-

sets. However, it was still observed that there were discrepancies between individual overlapping SARtopo profiles within swaths, altimetry profiles, and DTMs (see SOM). To minimize these differences between overlaps, we ran a second order correction using a global least squares minimization on a profile-by-profile basis to remove the relative offsets between the SARtopo, altimetry and DTM datasets. We determined that 160 of the 191 profiles between SARtopo and altimetry overlapped and could therefore be minimized together. The remaining profiles that did not intersect any other could not be minimized and were left unshifted. The final offsets between these profiles follow a Gaussian distribution centered about zero and a standard deviation of ∼80m. After the profile-by-profile minimization is performed, the DTMs are then tied down to the minimized SARtopo data at 32 pixels-per-degree (32PPD) by allowing both an offset and 2D tip-tilt to be applied to each DTM. This tip-tilt is determined by fitting a plane to the difference between the DTM and altimetry/SARtopo at the points where they overlap. The plane is then subtracted from the DTM to minimize the offsets between the datasets. A final minimization is re-run with the corrected DTMs to obtain one final set of minimized offsets between all the data products. We find the minimization further reduced the average offset between the datasets by ∼30%.

2.4. Spherical Harmonic Fitting

We model the shape of Titan using a spherical harmonic decomposition. To do so we use a weighted least squares approach to find the best fit coefficients for the complex spherical harmonics through 8^{th} order to the measured topographic data. Order 8 was chosen as this was the highest order for which there was sufficient sampling across Titan's

surface (see Figure 1). As a result of the minimization process, errors were taken to be independent, and no additional correlation (i.e. off-diagonal) terms were used in the covariance matrix for the best fit solution. Details of the fitting can be found in the SOM. The derived coefficients for the spherical harmonic expansion can be found in Table 1.

2.5. Error Estimation

Error maps for each profile were generated at the 32PPD scale and added in quadrature to the 4PPD of the interpolation. The application of the minimization described above acts to reduce correlations observed along profiles and to minimize additional systematic errors and biases that result from ephemeris and pointing uncertainty. Regardless, both uncorrelated and correlated errors are taken into account during the error estimation.

To understand the effects of these errors, we ran a Monte Carlo simulation of one thousand realizations at 1PPD for the topography interpolation and 4PPD for the spherical harmonic fitting. For each realization, a modulated dataset was created in two steps. First, a systematic offset was selected for each flyby drawn from appropriate Gaussian distributions with standard deviations equal to the average systematic error for each flyby. Second, each observation point was further modulated using the same approach, but with a standard deviation corresponding to the uncorrelated random error in the individual measurement. Error maps were then created using the standard deviation of the resulting interpolations for both Titan's topography and shape and are displayed in Figure 1. The same process was used for generating the error in the spherical harmonic coefficients and best fit shape of Titan, except at the higher 4PPD. This approach is conservative as the

true error after minimization lies between the unminimized random and systematic errors used in the error estimation.

3. Results

The final maps of Titan's topography and shape can be found in Figures 2 & 3, respectively. We further provide an equicylindrical projection of the geoid corrected map in the SOM. All maps (both with and without geoid correction for use with hydrology studies), along with their associated errors (see Figure 1), are provided for the community as data files in the SOM.

4. Discussion

Our interpolated topography can now be used to understand surface-atmosphere interactions, surface transport processes, and geophysical processes. This dataset can also be used as an input to various models that will attempt to understand these processes and interactions on Titan (e.g., [*Neish et al.*, 2016; *Howard et al.*, 2016]). Below we provide an initial qualitative overview of the new features in the topographic data.

4.1. Surface Geology and Liquid Distribution

Currently, the largest liquid bodies on Titan are the three northern filled seas, which occupy local topographic lows; similar basins are also observed at the south pole [*Hayes et al.*, 2011; *Birch et al.*, 2017]. Recent work has suggested these sites to be the locations of seas in the geologically recent past [*Birch et al.*, 2017]. Further, our topography shows that the previously identified equatorial basins, Tui and Hotei Regiones, are also closed basins like their northern and southern counterparts. This supports the hypothesis that these

regions were also formerly filled liquid basins [*Moore and Howard*, 2010]. Additionally, the new topographic map shows that Titan's small lakes are within local topographic lows that themselves are contained within the higher standing terrains at both poles, supporting a similar hypothesis in *Birch et al.* [2017] using geomorphologic mapping. At finer scales, these basins are completely enclosed [*Hayes et al.*, 2017 in press], suggesting a different evolutionary history than the larger seas [*Hayes*, 2016].

Further, surface wind patterns can be inferred through Titan's dune morphologies and orientations [*Tokano*, 2010; *Charnay et al.*, 2015]. Titan's equatorial dunes are known to diverge around topographic obstacles and are likely influenced by local topographic slopes at their margins [*Lorenz and Radebaugh*, 2009]. Counter-intuitively, our map shows that Titan's dunes correlate well with topographic highs over Titan's equatorial regions.

4.2. General Circulations Models

Topographic maps provide insights into GCMs through understanding the interaction between the surface and atmosphere and the roles this can play on global wind patterns, super-rotation in the stratosphere, convective clouds formation, and availability of surface liquids. To date, these models have mostly assumed a flat topography [*Lora et al.*, 2015; *Newman et al.*, 2016], even though initial work suggests that the topography should have significant influences on the model results (pers.comm. J.Lora, C.Newman). For example, improved understanding of mountainous terrains, such as at the south pole, would provide additional constraints on atmospheric phenomena such as orographic forcing of gravity waves [*Lora et al.*, 2015]. Another application is the incorporation of surface runoff [*Newman et al.*, 2016], estimated from topography, to better predict the location

of surface liquids in the GCMs [*Horvath et al.*, 2016], which has been shown to have significant effects in the potential evolutionary tracks of Titan's climate [*Lora et al.*, 2015]. An accurate understanding of topography, therefore, can also provide better understanding of atmospheric and surface patterns which can then be incorporated into (and tested against) GCMs.

4.3. Geophysical Relations

We observed several general observations on the shape and global-scale topography of Titan. We confirm the four previously identified topographic rises in Titan's southern hemisphere at ∼45°S, 330°E [*Lorenz et al.*, 2013] and identify fifth rise potentially associated with these. This fifth additional rise could suggest the presence of a larger, quasi-linear mountain range that extends across Titan's southern mid-latitudes. This ridge accentuates the overall asymmetry in Titan's southern hemisphere topography. Further, the southeastern hemisphere sits ∼200m lower than the southwestern hemisphere, a dichotomy not observed in Titan's northern hemisphere. The origin and implications of this dichotomy is beyond the scope of this paper.

Xanadu, a prominent, enigmatic SAR-bright terrain in Titan's equatorial region is found to be a higher than measured by *Lorenz et al.* [2013] by ∼125m. However, Xanadu remains a local low relative to its surroundings [*Stiles et al.*, 2009; *Radebaugh et al.*, 2011; *Lorenz et al.*, 2013], which include the Shangri-La and Fensal dune fields. This is counter-intuitive as it is expected that a local topographic depression should fill with aeolian sands, yet this is not the case. This suggests an anomalous behaviour where the absence of aeolian dunes may result from periodic wetting and drying within Xanadu and/or unresolved

morphologic/topographic features (ex., fluvial networks [*Barnes et al.*, 2015]). Thus, the origin of Xanadu and its topographic/morphologic relationship with surrounding terrains remains inconclusive.

Finally, from the derived spherical harmonic coefficients for the shape of Titan, we find the principal axes of the shape tri-axial ellipsoid defined as:

$$a = C_{00} - \frac{1}{2}C_{20} + 3C_{22} = 2575.124 \pm .026km \tag{1}$$

$$b = C_{00} - \frac{1}{2}C_{20} - 3C_{22} = 2574.746 \pm .045km \tag{2}$$

$$c = C_{00} + C20 = 2574.415 \pm .028km \tag{3}$$

The values derived from the fit of a triaxial ellipsoid to the new topography are a=2575.164±.013km, b=2574.720±.024km, c=2574.314±.029km. The discrepencies between the two derivations can be explained by the contribution from higher order harmonics that result from the non-uniformly sampled topographic data. We find a mean radius of Titan to be R=2574.765±.018km, a polar flattening of f=(a-c)/a = 1/(3632±202), and hydrostatic parameter h=(a-c)/(b-c) = 2.14±.38. The newly measured flattening is higher than measured by *Mitri et al.* [2014] and the hydrostatic parameter deviates slightly more from hydrostatic equilibrium, corresponding to h=4. This suggests an even greater amount of hydrostatic compensation is required from the ice shell [*Mitri et al.*, 2014] to match the gravity field and remain consistent with hydrostatic equilibrium [*Iess*

et al., 2010, 2012]. One possible solution to this disagreement is that perhaps the latitudinal variations in the thickness of Titan's ice shell are greater than previously measured by *Nimmo and Bills* [2010].

5. Conclusions

We present updated topographic and spherical harmonic maps of Titan making use of the complete Cassini RADAR dataset for use by the scientific community. These maps improve on previous efforts [*Lorenz et al.*, 2013; *Mitri et al.*, 2014] through their increased coverage, higher resolutions, a global minimization of the data, and incorporation of observational errors, with the intent to serve a broader range of studies within the Titan community.

Several notable correlations and improvements can be found in the new topography. First, we find a correlation between potential ancient and current liquid bodies within local depressions. Second, is the correlation with the dunes and topographic highs in Titan's equatorial region. Third, we note an additional topographic rise located at ∼45°S, 330°E, which correlates with the previously identified mountain chain in this region. Fourth, is the asymmetry in the shape of Titan's south pole with a high eastern hemisphere and a low western hemisphere. Fifth, Xanadu is now measured to be higher than before, but is still a local depression. Finally, the shape of Titan is updated and found to be slightly more non-hydrostatic than previously measured.

6. Acknowledgements

PC and SPDB acknowledge funding for this work by the NASA Earth and Space Science Fellowship Program: Grant Numbers NNX14AO31H S03 and NNX15AQ87H S03, respec-

tively. AGH acknowledges funding for this work form Grant Number NNX15AH10G. This research was also supported by the Cassini-Huygens mission, a cooperative endeavor of NASA, ESA, and ASI managed by JPL/Caltech under a contract with NASA. We further acknowledge the Spacecraft Planetary and Imaging Facility (SPIF) for support and resources in generating the topographic data products.

Data can be found in the SOM of this article and are available from the corresponding author upon request. Further, the data can be found at http://hayesresearchgroup.com/data-products/.

References

Barnes, J. W., R. D. Lorenz, J. Radebaugh, A. G. Hayes, K. Arnold, and C. Chandler (2015), Production and global transport of Titan's sand particles, *Planetary Science*, *4*, 1, doi:10.1186/s13535-015-0004-y.

Birch, S. P. D., A. G. Hayes, W. E. Dietrich, A. D. Howard, C. S. Bristow, M. J. Malaska, J. M. Moore, M. Mastrogiuseppe, J. D. Hofgartner, D. A. Williams, O. L. White, J. M. Soderblom, J. W. Barnes, E. P. Turtle, J. I. Lunine, C. A. Wood, C. D. Neish, R. L. Kirk, E. R. Stofan, R. D. Lorenz, and R. M. C. Lopes (2017), Geomorphologic mapping of titan's polar terrains: Constraining surface processes and landscape evolution, *Icarus*, *282*, 214–236, doi:10.1016/j.icarus.2016.08.003.

Broomhead, D., and D. Lowe (1988), Multivariable functional interpolation and adaptive networks, *Complex Systems*, *2*, 321–355.

Burr, D. M., S. A. Drummond, R. Cartwright, B. A. Black, and J. T. Perron (2013), Morphology of fluvial networks on Titan: Evidence for structural control, *Icarus*, *226*,

742–759, doi:10.1016/j.icarus.2013.06.016.

Cartwright, R., J. A. Clayton, and R. L. Kirk (2011), Channel morphometry, sediment transport, and implications for tectonic activity and surficial ages of Titan basins, *Icarus*, *214*, 561–570, doi:10.1016/j.icarus.2011.03.011.

Charnay, B., E. Barth, S. Rafkin, C. Narteau, S. Lebonnois, S. Rodriguez, S. Courrech Du Pont, and A. Lucas (2015), Methane storms as a driver of Titan's dune orientation, *Nature Geoscience*, *8*, 362–366, doi:10.1038/ngeo2406.

Elachi, C., M. D. Allison, L. Borgarelli, P. Encrenaz, E. Im, M. A. Janssen, W. T. K. Johnson, R. L. Kirk, R. D. Lorenz, J. I. Lunine, D. O. Muhleman, S. J. Ostro, G. Picardi, F. Posa, C. G. Rapley, L. E. Roth, R. Seu, L. A. Soderblom, S. Vetrella, S. D. Wall, C. A. Wood, and H. A. Zebker (2004), Radar: The Cassini Titan Radar Mapper, *Space Science Review*, *115*, 71–110, doi:10.1007/s11214-004-1438-9.

Griffith, C. A., P. Penteado, S. Rodriguez, S. Le Mouélic, K. H. Baines, B. Buratti, R. Clark, P. Nicholson, R. Jaumann, and C. Sotin (2009), Characterization of Clouds in Titan's Tropical Atmosphere, *Astrophysical Jounral Letters*, *702*, L105–L109, doi: 10.1088/0004-637X/702/2/L105.

Hayes, A., O. Aharonson, P. Callahan, C. Elachi, Y. Gim, R. Kirk, K. Lewis, R. Lopes, R. Lorenz, J. Lunine, K. Mitchell, G. Mitri, E. Stofan, and S. Wall (2008), Hydrocarbon lakes on Titan: Distribution and interaction with a porous regolith, *Geophysics Research Letters*, *35*, L09204, doi:10.1029/2008GL033409.

Hayes, A. G. (2016), The Lakes and Seas of Titan, *Annual Review of Earth and Planetary Sciences*, *44*, 57–83, doi:10.1146/annurev-earth-060115-012247.

Hayes, A. G., O. Aharonson, J. I. Lunine, R. L. Kirk, H. A. Zebker, L. C. Wye, R. D. Lorenz, E. P. Turtle, P. Paillou, G. Mitri, S. D. Wall, E. R. Stofan, K. L. Mitchell, C. Elachi, and Cassini Radar Team (2011), Transient surface liquid in Titan's polar regions from Cassini, *Icarus*, *211*, 655–671, doi:10.1016/j.icarus.2010.08.017.

Hayes, A. G., S. D. Birch, W. E. Dietrich, A. D. Howard, R. L. Kirk, V. Poggiali, M. Mastrogiuseppe, R. J. Michaelides, P. M. Corlies, J. M. Moore, M. J. Malaska, K. L. Mitchell, R. D. Lorenz, and C. A. Wood (2017 in press), Topographic Constraints on the Evolution and Connectivity of Titan's Lacustrine Basins, *Geophysical Research Letters*.

Horvath, D. G., J. C. Andrews-Hanna, C. E. Newman, K. L. Mitchell, and B. W. Stiles (2016), The influence of subsurface flow on lake formation and north polar lake distribution on Titan, *Icarus*, *277*, 103–124, doi:10.1016/j.icarus.2016.04.042.

Howard, A. D., S. Breton, and J. M. Moore (2016), Formation of gravel pavements during fluvial erosion as an explanation for persistence of ancient cratered terrain on Titan and Mars, *Icarus*, *270*, 100–113, doi:10.1016/j.icarus.2015.05.034.

Iess, L., N. J. Rappaport, R. A. Jacobson, P. Racioppa, D. J. Stevenson, P. Tortora, J. W. Armstrong, and S. W. Asmar (2010), Gravity Field, Shape, and Moment of Inertia of Titan, *Science*, *327*, 1367, doi:10.1126/science.1182583.

Iess, L., R. A. Jacobson, M. Ducci, D. J. Stevenson, J. I. Lunine, J. W. Armstrong, S. W. Asmar, P. Racioppa, N. J. Rappaport, and P. Tortora (2012), The Tides of Titan, *Science*, *337*, 457, doi:10.1126/science.1219631.

Kirk, R. L., E. Howington-Kraus, B. Redding, P. S. Callahan, A. G. Hayes, A. Legall, R. M. C. Lopes, R. D. Lorenz, A. Lucas, K. L. Mitchell, C. D. Neish, O. Aharonson, J. Radebaugh, B. W. Stiles, E. R. Stofan, S. D. Wall, C. A. Wood, and Cassini RADAR Team (2012), Topographic Mapping of Titan: Latest Results, in *Lunar and Planetary Science Conference*, *Lunar and Planetary Science Conference*, vol. 43, p. 2759.

Krige, D. G. (1951), A statistical approach to some basic mine valuation problems on the Witwatersrand, *Journal of the Chemical, Metallurgical and Mining Society*, *52*, 119–139, doi:10.2307/3006914.

Lora, J. M., J. I. Lunine, and J. L. Russell (2015), GCM simulations of Titan's middle and lower atmosphere and comparison to observations, *Icarus*, *250*, 516–528, doi:10.1016/j.icarus.2014.12.030.

Lorenz, R. D., and J. Radebaugh (2009), Global pattern of Titan's dunes: Radar survey from the Cassini prime mission, *Geophysical Research Letters*, *36*, L03202, doi:10.1029/2008GL036850.

Lorenz, R. D., R. M. Lopes, F. Paganelli, J. I. Lunine, R. L. Kirk, K. L. Mitchell, L. A. Soderblom, E. R. Stofan, G. Ori, M. Myers, H. Miyamoto, J. Radebaugh, B. Stiles, S. D. Wall, C. A. Wood, and The Cassini Radar Team (2008), Fluvial channels on Titan: Initial Cassini RADAR observations, *Planetary and Space Science*, *56*, 1132–1144, doi:10.1016/j.pss.2008.02.009.

Lorenz, R. D., B. W. Stiles, O. Aharonson, A. Lucas, A. G. Hayes, R. L. Kirk, H. A. Zebker, E. P. Turtle, C. D. Neish, E. R. Stofan, and J. W. Barnes (2013), A global topographic map of Titan, *Icarus*, *225*, 367–377, doi:10.1016/j.icarus.2013.04.002.

Matheron, G. (1963), Principles of geostatistics, *Economic Geology*, *58*, 1246, doi: 10.2113/gsecongeo.58.8.1246.

Mitri, G., R. Meriggiola, A. Hayes, A. Lefevre, G. Tobie, A. Genova, J. I. Lunine, and H. Zebker (2014), Shape, topography, gravity anomalies and tidal deformation of Titan, *Icarus*, *236*, 169–177, doi:10.1016/j.icarus.2014.03.018.

Moore, J. M., and A. D. Howard (2010), Are the basins of Titan's Hotei Regio and Tui Regio sites of former low latitude seas?, *Geophysical Research Letters*, *37*, L22205, doi:10.1029/2010GL045234.

Neish, C. D., J. L. Molaro, J. M. Lora, A. D. Howard, R. L. Kirk, P. Schenk, V. J. Bray, and R. D. Lorenz (2016), Fluvial erosion as a mechanism for crater modification on Titan, *Icarus*, *270*, 114–129, doi:10.1016/j.icarus.2015.07.022.

Newman, C. E., M. I. Richardson, Y. Lian, and C. Lee (2016), Simulating Titan's methane cycle with the TitanWRF General Circulation Model, *Icarus*, *267*, 106–134, doi:10.1016/j.icarus.2015.11.028.

Nimmo, F., and B. G. Bills (2010), Shell thickness variations and the long-wavelength topography of Titan, *Icarus*, *208*, 896–904, doi:10.1016/j.icarus.2010.02.020.

Powell, M. J. D. (1977), Restart procedures for the conjugate gradient method, *Mathematical Programming*, *12*(1), 241–254, doi:10.1007/BF01593790.

Radebaugh, J., R. D. Lorenz, R. L. Kirk, J. I. Lunine, E. R. Stofan, R. M. C. Lopes, S. D. Wall, and the Cassini Radar Team (2007), Mountains on Titan observed by Cassini Radar, *Icarus*, *192*, 77–91, doi:10.1016/j.icarus.2007.06.020.

Radebaugh, J., R. D. Lorenz, J. I. Lunine, S. D. Wall, G. Boubin, E. Reffet, R. L. Kirk, R. M. Lopes, E. R. Stofan, L. Soderblom, M. Allison, M. Janssen, P. Paillou, P. Callahan, C. Spencer, and the Cassini Radar Team (2008), Dunes on Titan observed by Cassini Radar, *Icarus*, *194*, 690–703, doi:10.1016/j.icarus.2007.10.015.

Radebaugh, J., R. D. Lorenz, S. D. Wall, R. L. Kirk, C. A. Wood, J. I. Lunine, E. R. Stofan, R. M. C. Lopes, P. Valora, T. G. Farr, A. Hayes, B. Stiles, G. Mitri, H. Zebker, M. Janssen, L. Wye, A. LeGall, K. L. Mitchell, F. Paganelli, R. D. West, E. L. Schaller, and Cassini Radar Team (2011), Regional geomorphology and history of Titan's Xanadu province, *Icarus*, *211*, 672–685, doi:10.1016/j.icarus.2010.07.022.

Rafkin, S. C. R., and E. L. Barth (2015), Environmental control of deep convective clouds on Titan: The combined effect of CAPE and wind shear on storm dynamics, morphology, and lifetime, *Journal of Geophysical Research (Planets)*, *120*, 739–759, doi:10.1002/2014JE004749.

Rippa, S. (1999), An algorithm for selecting a good value for the parameter c in radial basis function interpolation, *Advances in Computational Mathematics*, *11*(2), 193–210, doi:10.1023/A:1018975909870.

Stiles, B. W., S. Hensley, Y. Gim, D. M. Bates, R. L. Kirk, A. Hayes, J. Radebaugh, R. D. Lorenz, K. L. Mitchell, P. S. Callahan, H. Zebker, W. T. K. Johnson, S. D. Wall, J. I. Lunine, C. A. Wood, M. Janssen, F. Pelletier, R. D. West, C. Veeramacheneni, and The Cassini Radar Team (2009), Determining Titan surface topography from Cassini SAR data, *Icarus*, *202*, 584–598, doi:10.1016/j.icarus.2009.03.032.

Stofan, E. R., C. Elachi, J. I. Lunine, R. D. Lorenz, B. Stiles, K. L. Mitchell, S. Ostro, L. Soderblom, C. Wood, H. Zebker, S. Wall, M. Janssen, R. Kirk, R. Lopes, F. Paganelli, J. Radebaugh, L. Wye, Y. Anderson, M. Allison, R. Boehmer, P. Callahan, P. Encrenaz, E. Flamini, G. Francescetti, Y. Gim, G. Hamilton, S. Hensley, W. T. K. Johnson, K. Kelleher, D. Muhleman, P. Paillou, G. Picardi, F. Posa, L. Roth, R. Seu, S. Shaffer, S. Vetrella, and R. West (2007), The lakes of Titan, *Nature*, *445*, 61–64, doi:10.1038/nature05438.

Tokano, T. (2010), Relevance of fast westerlies at equinox for the eastward elongation of Titan's dunes, *Aeolian Research*, *2*, 113–127, doi:10.1016/j.aeolia.2010.04.003.

Zebker, H. A., B. Stiles, S. Hensley, R. Lorenz, R. L. Kirk, and J. Lunine (2009a), Size and Shape of Saturn's Moon Titan, *Science*, *324*, 921, doi:10.1126/science.1168905.

Zebker, H. A., Y. Gim, P. Callahan, S. Hensley, R. Lorenz, and Cassini Radar Team (2009b), Analysis and interpretation of Cassini Titan radar altimeter echoes, *Icarus*, *200*, 240–255, doi:10.1016/j.icarus.2008.10.023.

Table 1. Spherical harmonic expansion coefficients of Titan's shape through 4^{th} order[a].

	Value	$\pm 1\sigma$
C_{00}	2574761.7214	17.8378
C_{10}	10.7332	26.2639
C_{11}	22.2617	21.1719
C_{1-1}	1.6810	27.5294
C_{20}	-346.2728	23.8906
C_{21}	-4.8914	13.4222
C_{2-1}	17.8013	26.6987
C_{22}	62.9706	9.7188
C_{2-2}	4.3276	6.3238
C_{30}	12.3088	30.5568
C_{31}	49.2596	8.4291
C_{3-1}	50.8515	12.2129
C_{32}	-5.7497	5.1274
C_{3-2}	0.8929	3.7320
C_{33}	5.5922	1.3473
C_{3-3}	-0.4440	1.5390
C_{40}	-165.3450	36.4908
C_{41}	3.5949	7.5259
C_{4-1}	76.4667	12.6529
C_{42}	-2.7610	2.6539
C_{4-2}	-4.6973	2.0834
C_{43}	2.1330	0.6943
C_{4-3}	-2.1751	0.7962
C_{44}	-0.2598	0.2246
C_{4-4}	-1.0385	0.1670

[a]The remainder of the coefficients through 8^{th} can be found in the SOM.

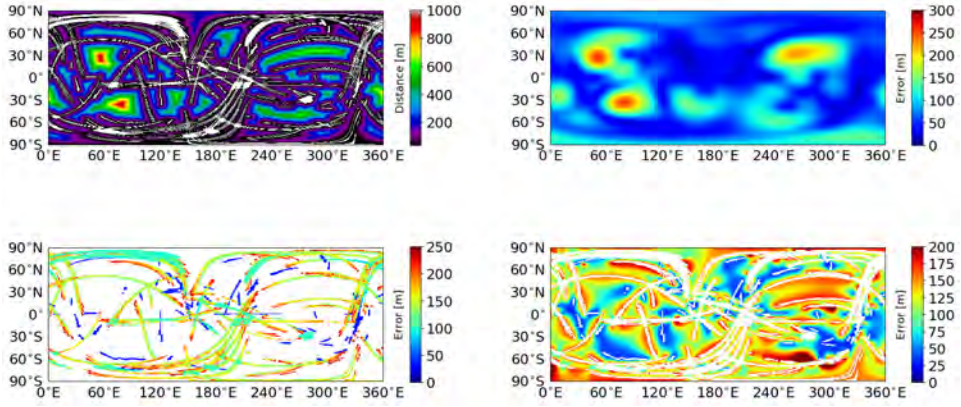

Figure 1. Top Left: Equicylindrical projection of the distance to the nearest measured data point. The largest separation is ∼1000km, corresponding to ∼22°. The average separation distance is ∼175km or ∼4°. Top Right: Estimates of the error in the spherical harmonic fitting to 8th order using a Monte Carlo approximation. Bottom Left: Error in the topography at 1°x1° resolution used as inputs to the Monte Carlo simulation. The greatest error is found at the beginning and end of SARtopo swaths. The lowest error is associated with altimetry measurements. For SARtopo the error used is the systematic error of ∼160m, which is larger than the relative error of ∼50m along a given profile. The post-minimization errors, therefore, should lie between these values and thus we take a conservative estimate. Bottom Right: Errors on the minimized interpolations from Monte Carlo simulations. Regions of large interpolation are more insensitive to variations in the measured topography and so appear as large, smooth regions, of lower error compared to the input errors.

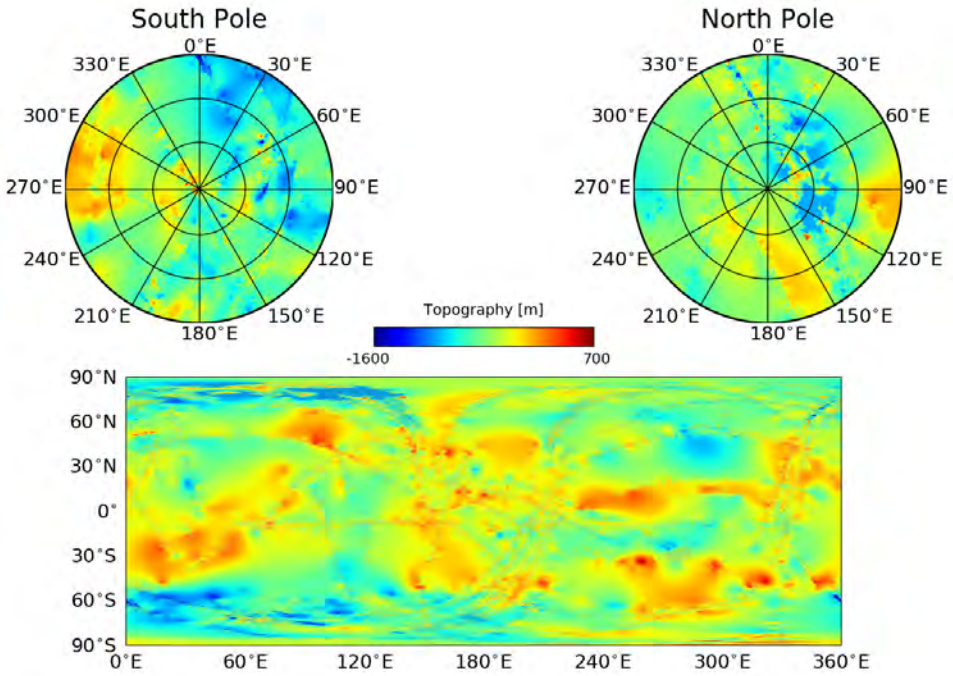

Figure 2. Top: Stereographic polar projections of Titan's topography with the South Pole left and the North Pole right. Ontario Lacus and the each of the large northern seas are found in local depressions. Bottom: Equicylindrical projection of Titan's topography. All maps have been corrected for the geoid, derived from the parameters defined in Table 1, SOL1a of *Iess et al.* [2012]. Regions of altimetry and SARtopo data that were used in the interpolation are over-plotted in grey. Most noteable is the asymmetry of the southern hemisphere. Xanadu is measured to be more elevated than previously measured by *Lorenz et al.* [2013], more similar to its antipodal complement.

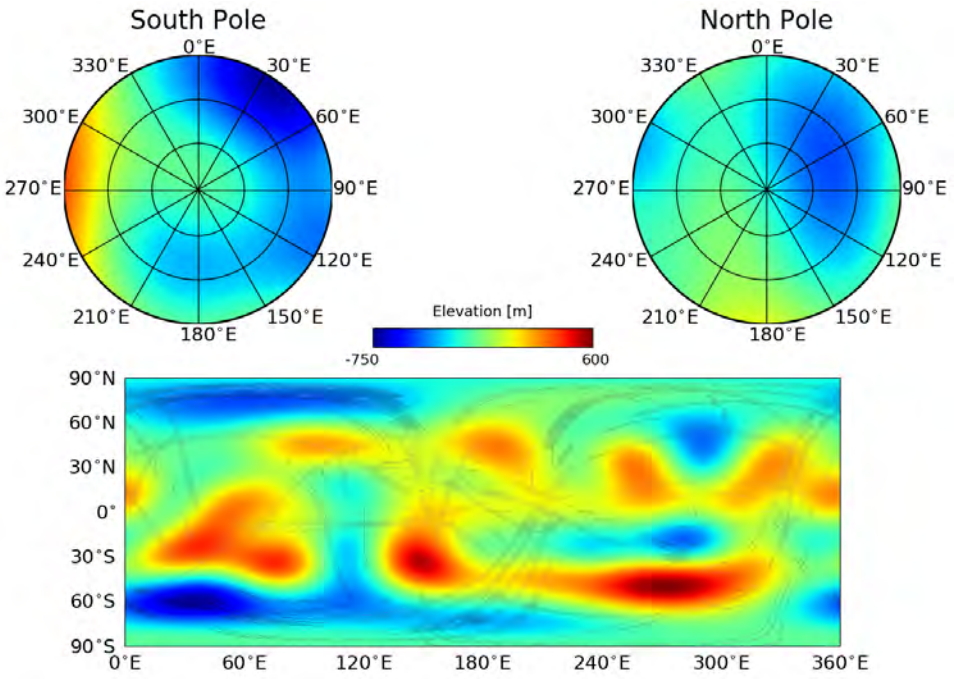

Figure 3. As in Figure 2 but using an 8^{th} order spherical harmonic fit to Titan's topography and corrected for the geoid. Large scale topographic variations are captured well. An 8^{th} order fit was chosen as it is the highest order for which there is global sampling in the topography dataset as determined from the distance between samplings (see Figure 1). Maps of individual orders can be found in the SOM.